X-ray computed micro tomography as complementary method for the characterization of activated porous ceramic preforms

S. Vasić
Technical Mineralogy Group, Institute of Mineralogy and Petrography, University of Fribourg, CH-1700 Fribourg, Switzerland; and EMPA, Swiss Federal Laboratories for Materials Testing and Research, Laboratory for High Performance Ceramics, CH-8600 Duebendorf, Switzerland

B. Grobéty
Technical Mineralogy Group, Institute of Mineralogy and Petrography, University of Fribourg, CH-1700 Fribourg, Switzerland

J. Kuebler[a)] and T. Graule
EMPA, Swiss Federal Laboratories for Materials Testing and Research, Laboratory for High Performance Ceramics, CH-8600 Duebendorf, Switzerland

L. Baumgartner
Institute of Mineralogy and Petrography, Earth Science, University of Lausanne, CH-1100 Lausanne, Switzerland

(Received 22 December 2006; accepted 20 February 2007)

X-ray computed micro tomography (CT) is an alternative technique to the classical methods such as mercury intrusion (MIP) and gas pycnometry (HP) to obtain the porosity, pore-size distribution, and density of porous materials. Besides the advantage of being a nondestructive method, it gives not only bulk properties, but also spatially resolved information. In the present work, uniaxially pressed porous alumina performs activated by titanium were analyzed with both the classical techniques and CT. The benefits and disadvantages of the applied measurement techniques were pointed out and discussed. With the generated data, development was proposed for an infiltration model under ideal conditions for the production of metal matrix composites (MMC) by pressureless melt infiltration of porous ceramic preforms. Therefore, the reliability of the results, received from different investigation techniques, was proved statistically and stereologically.

I. INTRODUCTION

There is an increasing interest in using metal matrix composites (MMC) in applications where materials must have properties common to both metals and ceramics, e.g., in energy technology or the automotive industry.[1–4] Several methods for the fabrication of MMC materials and their properties have been proposed.[5,6]

An elegant and cheap way to manufacture such composites is by pressureless infiltration of metal melts into porous oxide ceramic performs.[7,8] This fabrication route is, however, hampered by the nonwetting behavior of metallic liquids on most oxide ceramic surfaces.[9,10] Addition of reactive elements, e.g., titanium (Ti), into the preforms has been shown to improve the wettability of oxide ceramics, and thus a satisfactory pressureless infiltration can be achieved.[11,12] Although the mechanisms responsible for the activation are not well understood, it is obvious from preliminary experiments that the porosity and permeability of the porous performs as well as the activator particle distribution, e.g., the average distance between titanium particles, are key parameters for the infiltration process.[13] A detailed knowledge of the three-dimensional (3D) assembly relating to porosity, pore-size distribution, and arrangement of the Ti particles and their size distribution within the porous ceramic performs is therefore indispensable.

Mercury intrusion porosimetry (MIP), helium pycnometry (HP), mercury buoyancy (MB), and measurements of nitrogen adsorption [Brunauer–Emmett–Teller (BET)] are traditional methods for obtaining pore-size distribution, porosity, density values of porous bodies, and specific surface areas of used powders.[14–17] Drawbacks of these methods are that models have to be

[a)]Address all correspondence to this author.
e-mail: jakob.kuebler@empa.ch
DOI: 10.1557/JMR.2007.0181

assumed for the evaluation of the data, like cylindrical pores for MIP, and that the information is spatially not localized[18–20]; moreover, some of the methods are destructive (MB, MIP).[21–28] BET and HP usually give results superior to MB and MIP and have the advantage of being nondestructive. Spatially localized information about porosity and Ti-particle distribution can be obtained from scanning electron microscopy (SEM), but 3D reconstruction from SEM images is tedious and model dependent.[29,30] The main merits and disadvantages of MIP, HP, MB, and SEM have been pointed out and compared in several review papers.[31–33]

Computed x-ray micro tomography (CT) is an alternative and powerful tool for the simultaneous determination of porosity and the 3D visualization of pore network as well as particle morphology and spatial distribution. This method has the additional advantage of being nondestructive.[34–39] Limitations of the method are that part of the image treatment such as thresholding of calculated gray scale images and stereological data extraction such as the transformation of the CT data into microstructural parameters (particle diameters, porosity, etc.) are model dependent and may therefore affect the results. Quantitative CT data analysis can also be hampered by limitation in the computing power of PCs.[40–46]

The main goal of this investigation was the complete characterization of the porous ceramic performs by CT and to validate the technique using the results from the classical methods as benchmark. The porosity, pore size and its distribution, and spatial distribution of titanium as an activator within the preforms were determined.

II. MATERIALS AND METHODS

A. Powder characterization and preform preparation

The preforms were manufactured from a powder mixture consisting of alumina A100 (Alumina WSK120, Treibacher, Germany) and titanium T40 (Titanium Gd1-40, TLS Technik GmbH & Co., Althofen, Germany) or T200 (Titanium Gd1-200; TLS Technik GmbH & Co.), which served as the activator. The particle-size distributions of the starting powders were determined by laser diffraction (LD; Malvern MasterSizerX, Worcestershire, UK; range: 1.2–600 μm, accuracy ≤2%). A 2 mW He–Ne laser source was used with a wavelength $\lambda = 633$ ηm and a scattering angle range between 0.03° and 50°. The data treatment was made assuming spherical particles. The Coulter SA3100 Series (Miami, FL) was used for BET measurements.[28,29] Three LD and BET measurements of each powder were made, and the limiting size d for the 10% (d_{10}), 50% (d_{50}), and 90% (d_{90}) volume fractions of particles $<d$ are given (Table I).[24–26] The morphology of titanium particles was analyzed by scanning electron microscopy (SEM) using a FEI XL 30 Sirion (Eindhoven, The Netherlands) FEG instrument [Figs. 1(a) and 1(b)].

TABLE I. Particle size distributions and BET values for A100, T40, and T200 powders determined by LD and BET compared to CT for titanium particles.

	d_{10} (μm)	d_{50} (μm)	d_{90} (μm)	BET (m^2/g)
LD-A100	94	151	245	0.0482
LD-T40	44	54	73	0.0320
CT-T40	43	56	75	···
LD-T200	180	205	240	0.0182
CT-T200	145	192	214	···

Powder mixtures A100T40 and A100T200 were fabricated by mixing A100 and T40 or T200 powders. Five batches of mixtures A100T40 with increasing amounts of Ti ($i = 1$, 3, 5, 10, and 20 wt% of the powder mixture) were prepared and labeled A100T40-i. Identical mixtures with T200 were manufactured but with only three different activation contents ($i = 3$, 5, and 20 wt%, A100T200-i). To improve the mechanical behavior of the

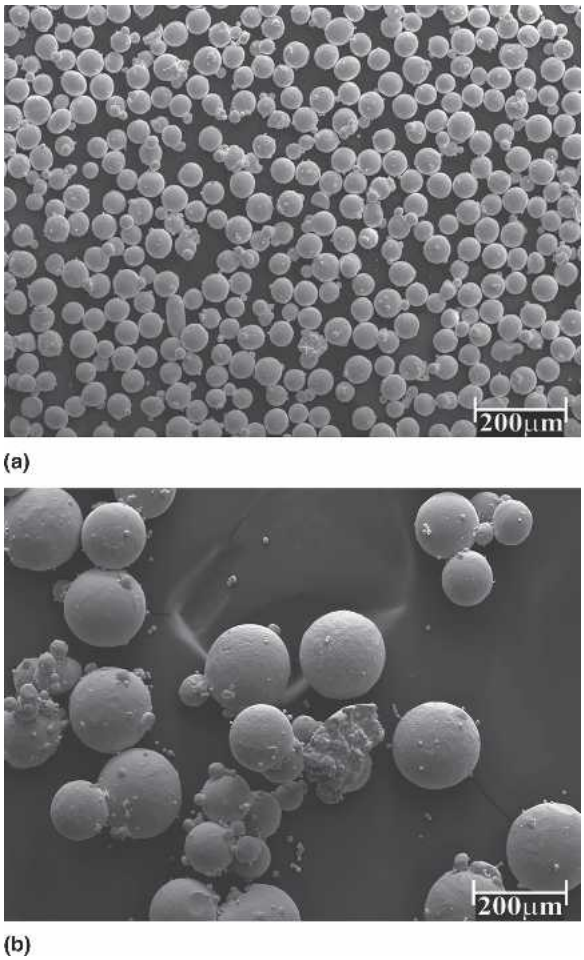

FIG. 1. Secondary electron images of titanium particles: (a) T40 and (b) T200. All particles are perfectly spherical. Note the formation of aggregates, especially by smaller particles.

https://doi.org/10.1557/jmr.2007.0181

preforms, 2 wt% binder BD (Natrium-Carboxymethylcellulose Octapix KG1000, Katadyn, Germany) was added to all batches. Binder and powders were dry mixed for 4 h in a ZoZ RM1 ball mill (Wenden, Germany) with 7-mm Al_2O_3 milling balls. After an addition of 10 wt% water, the mixing procedure was continued for another 20 h. To separate the powder from the milling balls, the mixtures were passed through a sieve with a 5-mm mesh. To see if milling had an effect on the titanium grain size distribution, a batch of T40 and T200 was milled for 15 h (Fig. 2). The cylindrical preforms 5 mm in diameter were fabricated by uniaxialy die pressing (Paul-Otto Weber press, Remshalden, Germany; 65 MPa) and subsequently dried at 50 °C for 24 h to get rid of the mixing water.

B. Preform characterization

MIP measurements were performed using a Porotec Pascal 140/440 Series porosimeter (Ithaca, NY) to obtain the open porosity π_O, apparent porosity π_A, and bulk density ρ_B of the porous preforms. The maximal pressure applied was 395 MPa, which corresponds to a minimum pore diameter D of 3.5 ηm. The pore-size distribution was extracted from the intrusion volume–pressure curve using the Pascal 140/440 Series software.[14–19] The total porosity π_T and solid density ρ_S of the preforms were obtained from Archimedes-principle based MB measurements with a Mettler AG204 Delta Range balance (Naenikon-Uster, Switzerland) adapted for buoyancy measurements. The main advantage of this method is that the open as well as the closed porosity is measured. The binder used in the present preforms is water soluble and precludes traditional buoyancy measurements. The determination of the open porosity π_O by HP was performed with the Micrometrics AccuPyc 1330 instrument (GA).[16,17,20] From each powder batch A100T40-*i* and A100T200-*i*, three samples were prepared and measured. For samples free of moisture and of volatile substances,

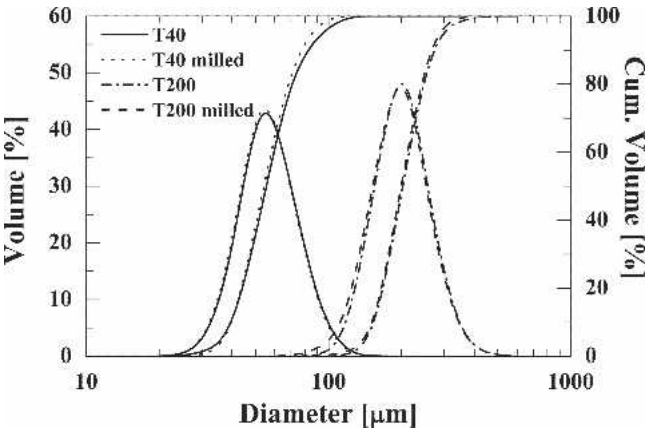

FIG. 2. Particle size distribution determined by LD for T40 and T200 particles before and after milling (15 h) shows no significant difference.

the skeletal density and open porosity may be determined with an error of ≤0.01%. All the above methods for microstructural characterization can be replaced by computed x-ray microtomography. This technique allows determination of bulk properties and gathering of localized information at the micron scale, which is essential to understand the factors controlling pressureless infiltration.[31,34,35,37–43] The measurement leaves the samples intact, and the infiltration experiments can be made on the same samples.

Absorption of x-ray in solids is a function of density, average atomic number, and thickness of the material and is described by Beer's law:

$$\frac{I}{I_0} = \exp(-\mu h) \quad , \tag{1}$$

where I_0 stands for the primary intensity, I for the measured intensity, μ the attenuation coefficient, and h the sample thickness. For a sample consisting of N different phases j, the exponential in Eq. (1) is given as sum of the individual attenuation coefficients times the corresponding thickness:

$$\frac{I}{I_0} = \exp\left(-\sum_{j=1}^{N} \mu_j h_j\right) \quad . \tag{2}$$

The attenuation coefficient μ is related to the absorption coefficient β, which is a function of density ρ and average atomic number Z:

$$\mu = \frac{4\pi\beta}{\lambda} \cong c\rho \frac{Z^4}{E^3} \quad , \tag{3}$$

where c is a constant and E the x-ray energy in keV. From Eq. (3) it is obvious that the absorption coefficient is very strongly dependent on the average atomic number ($\sim Z^4$) and is, therefore, well suited to map compositional changes in a sample. Alumina has an average atomic number of 10, and the atomic number of Ti is 22. The air, which fills the pores, has an average Z of 7.3. It is obvious that the other two phases can easily discriminate against Ti. The separation of air and alumina, despite the much higher density of the latter, causes more problems as their atomic numbers do not differ significantly. A 3D density map can be calculated from two-dimensional (2D) absorption sections. The images were recorded with a Skyscan 1072 Microtomograph (Skyscan, Kontich, Belgium). The operation conditions for the x-ray source were set at a voltage of 80 kV and current of 120 μA. The sample was rotated stepwise (0.9°/step) through 360°, and images were recorded at each step with an exposure time of 5 s. To minimize the noise, 8 frames per second were averaged. Sample recording took place at a magnification of 55×. The resolution in the backprojected images is about 6 μm. A 12-bit x-ray camera [charge-coupled device (CCD)] coupled to a scinilator

https://doi.org/10.1557/jmr.2007.0181

served as detector. The 2D transmission images were recorded on an area of 1024 × 1024 pixels [Figs. 3(a)–3(c)]. The choice of the measuring parameters e.g., $p = 400$ projections with $2q = 1024$ rays per projection (= 1024 pixels on the CCD camera) were chosen after testing different combinations of p and q. The ideal combination of p and q for the standard fan beam geometry is given by[44]

$$p = \pi q \quad . \tag{4}$$

The step size chosen is clearly too small compared to the value deduced from Eq. (4). The loss in resolution due to the undersampling in p is, however, acceptable, considering the gain in computation time.

Two samples for each A100T40-*i* and one for each A100T200-*i* mixture were analyzed. The result of the second A100T40-*i* series will not been shown in detail, but the comparison of the extracted microstructural data from the two series will be used to measure the representativity of the VOI. A total of 600 slices of reconstructed cross section images were combined to obtain a 3D model of a 4.95-mm-high section of the sample cylinder. Five volumes of interest (VOI), with a volume of 600 pixel × 600 pixel × 120 pixel = 3.3 mm × 3.3 mm × 0.66 mm, were fixed for the determination of the spatial distribution of the Ti particles and the determination of the particle size distribution [Figs. 4(a)–4(c)].

The size of the VOI is limited by the available computing power. It is obvious, that for the samples containing the coarse Ti particles (A100T200-*i*) the volume may be too small for an accurate particle size determination due to cutting effects. The primary goal of the CT analysis, however, was the determination of the spatial particle distribution, which is not influenced by the choice of the VOI volume. The particle size determination serves to check the validity of the data extraction procedure because the distribution is known from independent LD measurements.

The local structure of the pore network and the pore-size distributions are the other parameters controlling pressureless infiltration. The pore network can be extracted from the reconstructed 3D model of the samples. The same cylindrical pore network was used to transform the spatial 3D information values for bulk porosity and pore-size distribution as for the MIP data treatment. The latter data serve, similar to the particle size distribution data, as benchmarks for the validity of the CT data treatment.

The 3D reconstruction of the sample microstructure, as well as the extraction of bulk data, requires the processing of the raw CT transmission images taking into consideration statistical, stereological, and volumetric aspects. Several data procedure techniques have already been developed.[34–47] In the present work, the raw transmission images were backprojected using the ConeRec program from Skyscan,[38] which is based on a modified

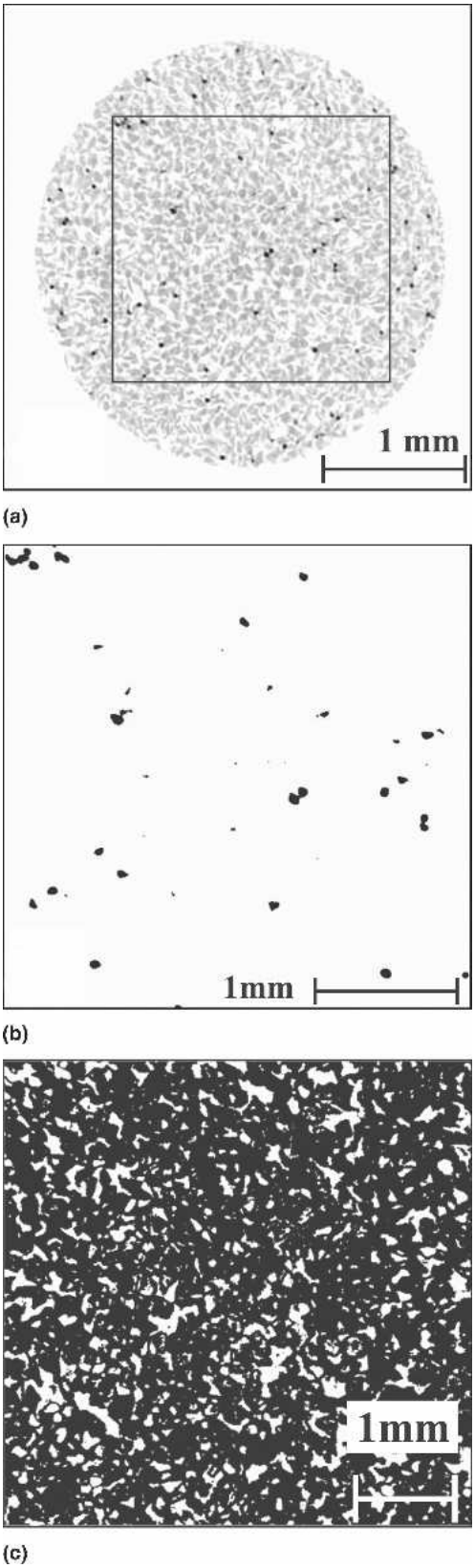

FIG. 3. (a) Backprojected transmission image. A region of interest (ROI) was chosen (rectangle) to avoid rim artifacts. The same ROI after thresholding is shown for (b) titania (black) and (c) pores (white).

https://doi.org/10.1557/jmr.2007.0181

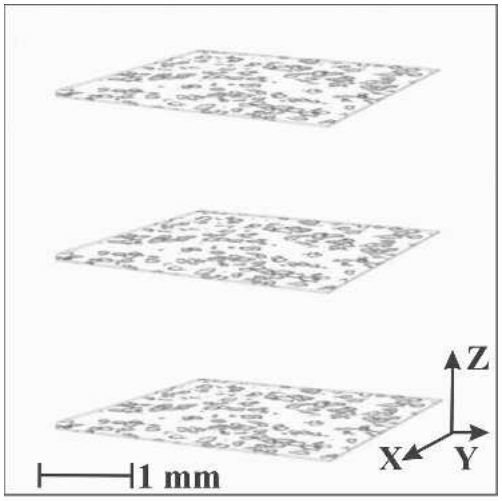

(a)

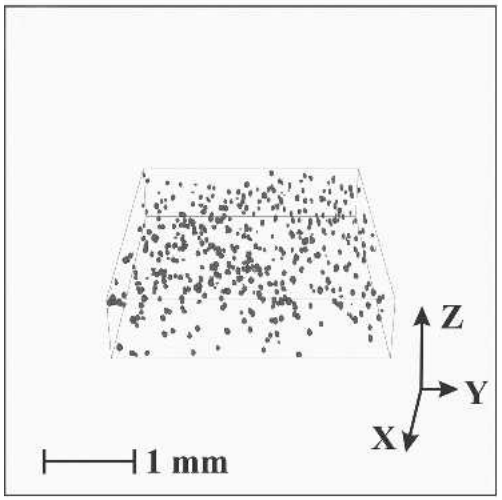

(b)

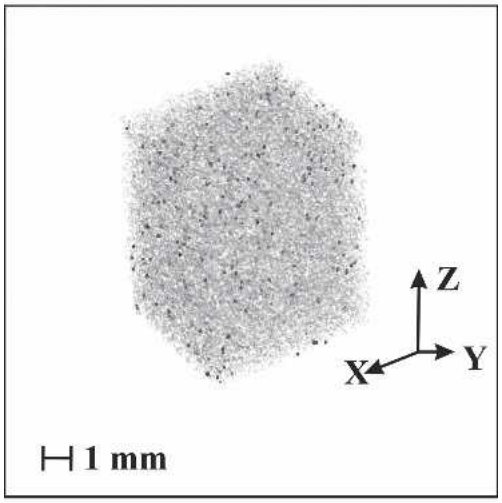

(c)

FIG. 4. (a) Schematic representation of a stack with three ROI sections and the corresponding 3D volume of interest (VOI) reconstructed (b) by Aphelion (black: Ti; VOI: 600 × 600 × 120 pixels) and (c) by ANT (Ti: black; Pores: gray; VOI. 600 × 600 × 900 pixels).

Feldkamp algorithm[48] [Fig. 3(a)]. Because the x-ray source is not strictly monochromatic, beam hardening and ring artifacts occur, which may bias the reconstructed density map. These artifacts are partially taken care of by the back projecting programs. Final adjustments were performed manually to obtain a constant gray scale level for each individual phase and to minimize the noise over the whole cross section of the sample. Brightness and contrast were adjusted, with care taken not to lose or add phase information. The contrast thresholds for the different phases were manually set from a gray tone level histogram. Titanium has the highest absorption and was attributed the highest gray level, e.g., black, whereas the air-filled pores were set to the lowest gray level, e.g., white. Within this contrast range, alumina has a light gray tone [Fig. 3(a)]. The processing time for a stack of 600 individual images was about 3 h [Figs. 4(a)–4(c)].

A program written with the Aphelion 3.2 software shell (TiParticles.apm, ADCIS, Hérouville Saint-Clair, France) was used for thresholding, filtering, and voxel information compilation[42,43][Figs. 3(a) and 3(b)]. The individual steps during the image processing were: thresholding of the different phases using the predefined gray tone level thresholds, convex cluster splitting, and voxel information compilation. The compiled voxels with gray levels corresponding to Ti were extracted from the 3D VOI after thresholding. Particles linked over bridges <4 pixels (~22 μm) for T40 particles and <18 pixels (~100 μm) for T200 were considered as aggregates and split. The bridge threshold is smaller than the smallest measured diameter for the Ti particles. The risk of an overall cluster splitting of nonspherical Ti particles is, therefore, small. Contiguous Ti voxels were attributed to a particle. The particles were numbered and characterized by voxel counts and 3D position coordinates of the center of gravity (x, y, z coordinates) within the VOI, which corresponds to the center, assuming spherical particles. The compiled voxels attributed to one particle were translated into sphere of equal volume, from which an equivalent sphere diameter was determined. From the coordinates of the center and of the surface envelope of each particle, the average interparticle distances were determined using a combined Excel/FORTRAN routine (Distance.dsw, The Fortran Company, Tucson, AZ). The same data were used to create a 3D presentation of spatial Ti particles distribution [ANT and Aphelion 3.2 software, Figs. 4(b) and 4(c)]. The voxel information for the volume occupied by pores was evaluated with Porosity-.apm, which is composed of the same steps as TiParticles.apm, except for the threshold value that was modified for the pores. Cluster splitting prevented pores from overlapping. The main source of error is the limited resolution of the backprojected image. The resolution is on the order of one pixel; the average error is, therefore, on the order of ±½ pixel.

https://doi.org/10.1557/jmr.2007.0181

Another method to check the reliability of the CT data is to compare the number of particles per unit volume obtained from 3D reconstruction of the VOI with the number derived from density measurements and calculated from 2D slices using Saltykov–Schwartz diameter analysis. Density-derived number counts were calculated using bulk densities as well as bulk porosities and assuming monodisperse population of Ti particles with a diameter corresponding to the average diameter of the real powder, e.g., 50 μm for T40 and 200 μm for T200.

The Saltykov–Schwartz algorithm was developed to extrapolate 3D particle size distribution as well as particle numbers per unit volume from particle contours present in 2D cross sections. It is also a valuable method for the appraisal of the procedure used for the 3D reconstruction from 2D-images.[46,47] The Saltykov method has been mainly discussed by Underwood et al.,[42,43] and is well suited to treating spherical particles. The Saltykov algorithm is based on the analysis of particle diameters in 2D sections, which are divided into m size intervals. The number of particles in each interval is $(N_A)_j$, where $j = 1, 2, \ldots\ldots k$, and the corresponding diameter range for the jth interval is $[D_{max}\cdot 10^{-0.1(j-2)} - D_{max}\cdot 10^{-0.1(j-1)}]$, where D_{max} is the largest 2D particle diameter observed in the examined sections. It is assumed that the diameter of the largest 2D particle is equal to that of the largest 3D spherical particle in the microstructure. The volumes of particles are also divided into the same number of identical intervals. With this assumption and the logarithmic scale for divisions of intervals, the 3D particle count $(N_V)_j$ per class j can be explicitly projected from $(N_A)_j$, according to the following equation:

$$(N_V)_j = \frac{D_{max}}{k} \sum_{j=1}^{k} \alpha_j (N_A)_j \quad . \tag{5}$$

The Saltykov parameters α_j were tabulated.[42,43] For each powder mixture, 120 slices were investigated. The full range of diameters was divided into 8 intervals for the A100T40-i samples and 15 intervals for the A100T200-i samples. The main disadvantage of the standard Saltykov method is that it generates negative values in several size classes, which in reality is impossible. The Saltykov F algorithm was used to overcome this problem.[49]

III. RESULTS AND DISCUSSION

A. Preform characterization

SEM analysis confirmed the spherical shape of the titanium particles (Fig. 1), facilitating the choice of particles. The LD measurements gave a unimodal and rather narrow particle size distribution for both T40 and T200 with d_{50} values at 54 and 205 μm, respectively (Table I, Fig. 2), which correspond well to those specified by the suppliers. The minimum diameters were 30 and 120 μm and the maximum diameters were 100 and 300 μm for the T40 and T200 particles, respectively. The detection limit of the LD instrument used (1.2 μm) was well below the smallest Ti particle diameters. Milling did not affect the particle size distribution of titanium; the differences between the distribution before and after, even prolonged milling times are negligible (Fig. 2). The particle size distributions of the bulk titanium powders were, therefore, used as the benchmark to compare the distributions obtained from CT measurements. Specific surface measurements yielded 0.0482, 0.0320, and 0.0182 m^2/g for A100, T40, and T200, respectively.

Density values of the preforms determined by MIP, MB, and HP were in the expected range. The average theoretical calculated skeletal density of the alumina/titanium compacts were between 3.995 g/cm^3 for $I = 1$ and 4.093 g/cm^3 for $I = 20$. For example the MB skeletal density for the mixture $i = 1$ was 3.95 g/cm^3, and for $i = 20$ it was 4.13 g/cm^3, values very close of the theoretical values, an indication that the mixtures were homogeneous at the sample size scale. The densities obtained from the same samples with 1 wt% Ti of the powder mixture by MIP and HP were $\rho_A = 4.01$ g/cm^3 and $\rho_A = 3.95$ g/cm^3, respectively, indicating that the closed porosity, which cannot be penetrated by mercury and nitrogen, was less than 4% of the total porosity (Table II).

The ~1.5 % larger value for HP was explainable by the fact that the intrusion behavior of nitrogen is better than mercury, and that the smallest pore size, which can be penetrated by mercury, is limited by the maximal pressure (395 MPa) attainable with the MIP instrumentation.

The bulk density $\rho_B = 2.34$ g/cm^3 from MIP as well as $\rho_B = 2.36$ g/cm^3 from HP matched well the theoretical bulk density of 2.50 g/cm^3 calculated from the skeletal density and the measured bulk porosity. The porosity of 43.38% determined by MB was the total porosity, e.g., open plus closed, whereas the values of 42.05% and 39.15% obtained from HP and MIP, respectively, represented the open porosity only. The MIP value was limited to pores larger than 3.5 nm.

TABLE II. Comparison of pore size, pore-size distributions, porosity, and density values determined by different methods for all powder mixtures A100T40-20 with the corresponding standard deviations SD (±). Each value consists of averaged 25 measurements, 5 for each powder mixture.

	MIP	CT	MB	HP
D (μm)	25.28 ± 1.64	24.91 ± 1.64	⋯	⋯
π_0 (%)	39.15 ± 0.64	⋯	⋯	42.05 ± 0.72
π_T (%)	⋯	40.01 ± 0.45	43.48 ± 0.67	⋯
$D < 10$ μm (%)	18.32 ± 0.83	16.65 ± 3.86	⋯	⋯
ρ_A (g/cm^3)	4.01 ± 0.08	⋯	⋯	3.95 ± 0.02
ρ_B (g/cm^3)	2.34 ± 0.07	⋯	⋯	2.36 ± 0.03
ρ_S (g/cm^3)	⋯	⋯	4.13 ± 0.32	⋯

https://doi.org/10.1557/jmr.2007.0181

Overall, the physical parameters of the powder compacts measured by the classical methods were consistent among themselves and also consistent with the bulk mixture recipe. They were therefore used as controls for the CT-derived values.

B. X-ray micro tomography

All CT-derived physical parameters were extracted from the five VOI. The data represent the properties of partial volumes of the samples. Differences with the data derived from classical methods may, therefore, be caused by inhomogeneities. The small standard deviation of the average properties obtained form the individual VOIs, however, was a good indication that the microstructure of the samples was homogeneous at the VOI scale. This was not true for data extracted from individual slices as will be shown for particle count, especially for the A100T200 sample.

The titanium particle size distribution was determined by averaging values obtained from 5 VOIs for each sample (Table I). While the results obtained for T40 matched well with the LD particle size measurements on the bulk powder, a shift to smaller values of the CT derived distribution was observed for T200 (Fig. 5).

The discrepancy was due to cutting effects at the VOI boundaries. For particles located across the boundary, only the volume inside the VOI was retained. The overall effect on the particle distribution was an increase in the volume fraction of small particles and a simultaneous decrease of the number of large particles. The location of the maximum was not affected. The shift was small for T40 and the distribution, and particle count was in excellent agreement with the results of the Saltykov algorithm (Fig. 6, Table III), which showed the same shift relative to the LD data.

The influence of the cutting effect on the 3D CT data and the Saltykov-derived data was thus similar. The larger shift for T200 was due to the larger particle size relative to the VOI. The VOI was thus clearly too small to determine a reliable particle size distribution in the A100T200 samples. The position and shape reconstruction of the individual particles, however, should not have been affected by the VOI size. The CT-derived number of particles per unit volume was in good

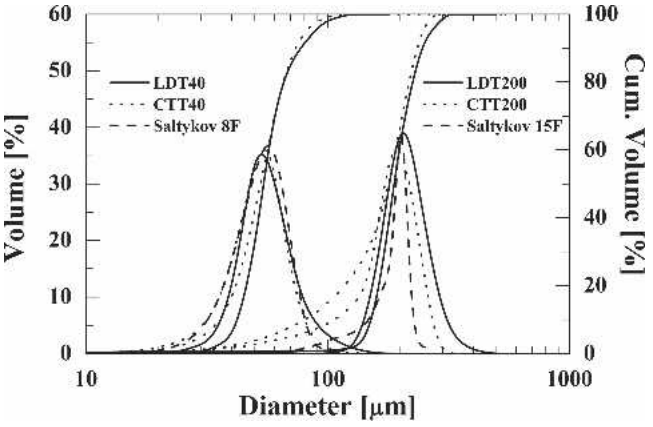

FIG. 5. Comparison of the particle size distributions determined by LD, CT, Saltykov 8F for T40, and Saltykov 15F for T200, respectively.

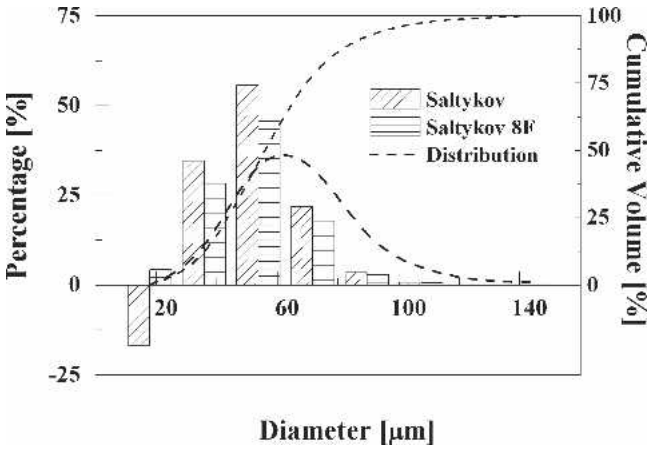

FIG. 6. Comparison of the particle size distribution calculated with the Saltykov and the Saltykov 8F algorithm. The curves show the distribution and the cumulative volume of the particles.

TABLE III. Particle-size distribution data for titanium particles determined by Saltykov diameter analysis, with 8 particle classes with regard to the LD measurements (120 Slices; A100T40-10).

Group no.	Range of section diameters (μm)	Number of sections per mm^2 $(N_A)_i$	Diameters of particles D_j (μm)	Number of particles per mm^3 $(N_V)_i$	Distribution (%)
1	0–17.19	0	17.19	11	1.87
2	17.19–34.38	7	34.38	81	14.23
3	34.38–51.56	14	51.56	289	50.64
4	51.56–68.75	8	68.75	166	29.14
5	68.75–85.94	1	58.94	20	3.47
6	85.94–103.13	0	103.13	3	0.53
7	103.13–120.31	0	120.31	1	0.09
8	120.31–137.5	0	137.5	0	0.03
Totals		30	5	571	100

https://doi.org/10.1557/jmr.2007.0181

TABLE IV. Number of particles (a) T40 and (b) T200 per mm^3 compared to different methods.

		CT	Saltykov 8F	Ideal
(a)	1% titanium	69	64	73
	3% titanium	121	123	111
	5% titanium	256	233	270
	10% titanium	433	453	460
	20% titanium	1202	1224	1250
		CT	Saltykov 15F	Ideal
(b)	3% titanium	8	7	7
	5% titanium	16	14	13
	20% titanium	50	55	48

agreement with the calculated particle counts, another sign for the reliability of the reconstruction procedure (Table IV).

The conversion of pore volume extracted from CT data into classic pore-size distribution representations depended on the choice of the pore model. A network of randomly distributed cylindrical pores was selected in the present study. The calculated distribution with a maximum at 40 μm matched well the data obtained by MIP, for which the same pore model was used [Fig. 7(a)]. Difficulties in setting the correct contrast threshold between alumina and air as well as the limited resolution of the tomograph (5.5 μm) were the most important errors in the location of pores, and they explained the shift of the CT pore-size distribution to larger values. The average pore size determined by CT was, nevertheless, very close to the MIP derived values [Table II, Fig. 7(b)].

Distances between the 10 nearest neighbor centers and surfaces were calculated as well as the first three nearest neighbors in relation to the activation content (Table V, Fig. 8). Both show an asymptotic behavior toward a constant value. The results are briefly summarized in Table V. The interparticle distances for the A100T40-*i* series could best be matched by a Poisson distribution function, a clear sign that the particles were randomly distributed. The particles distributions for the A100T200-*i* samples, however, were very noisy, which was mainly due to the low number of particles in the observed VOI. [Figs. 9(a)–9(d)].

The smooth interparticle distance distributions and the good correspondence between the microstructural parameters extracted from the two A100T40-*i* series

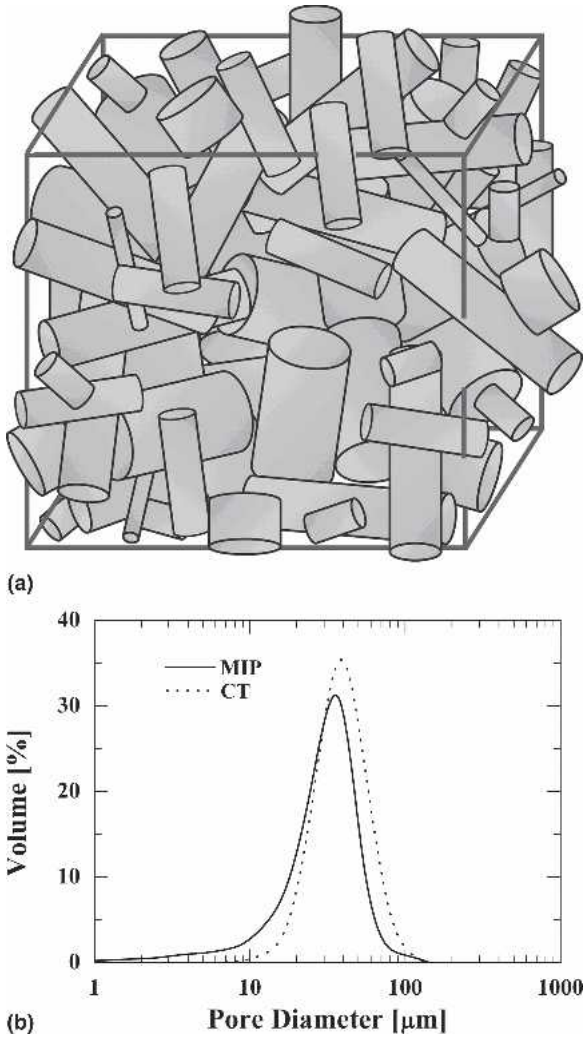

FIG. 7. (a) Schematic model applied for the determination of pore diameter and pore-size distribution by CT and (b) comparison of pore-size distribution determined by CT and MIP.

(Table V) and with the data extracted from the other methods was a good indication that the values were representative for the analyzed samples. For the A100T200-*i* samples, the VOI was smaller than the homogeneity length scale for the Ti-particle distribution of the whole sample. Because the overall sample size was not considerably larger than the VOI, the whole samples had to be considered inhomogeneous, and the data extracted from the VOI were valid only for the measured sample.

TABLE V. Nearest distances between particle neighbors from center to center as well as from particle surfaces in relation to different activation contents. For T40 particles two series (A/B) were calculated to show the representativity of the extracted data.

	Average minimal distance in (μm) between particles							
	T40-1 (A/B)	T40-3 (A/B)	T40-5 (A/B)	T40-10 (A/B)	T40-20 (A/B)	T200-3	T200-5	T200-20
Center	132/128	84/81	69/71	63/64	52/54	350	232	173
Surface	82/78	39/36	23/24	17/19	8/9	220	112	40

https://doi.org/10.1557/jmr.2007.0181

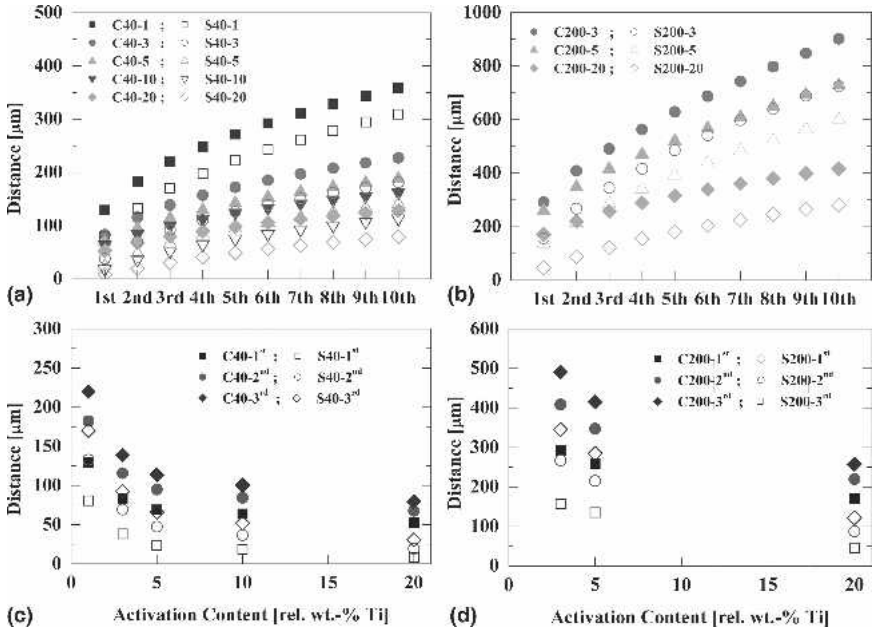

FIG. 8. Average distance between the 10 nearest neighbors (a) for T40 and (b) for T200 particles from particle centers (C) and surfaces (S). Distance among the first three nearest neighbors versus activation content for (c) T40 and (d) T200 particles.

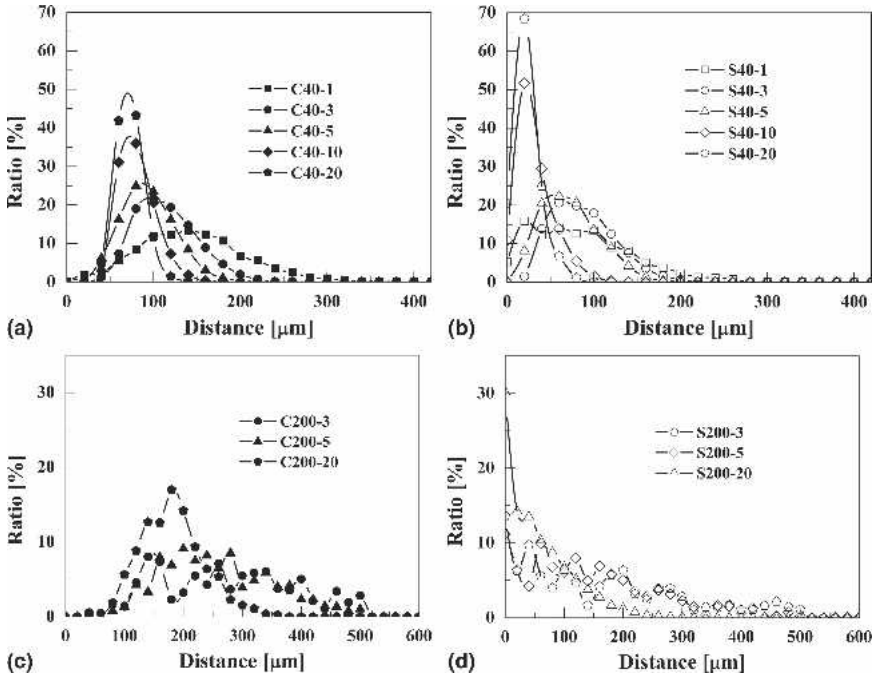

FIG. 9. Distance distribution among particle (a) centers (C) and (b) surfaces (S) for T40 and (c) center to center distances (C) as well as (d) surface to surface distance (S) distribution for T200.

IV. CONCLUSIONS

The analysis of porous ceramic performs has shown that data obtained by x-ray tomography not only can be used for the spatial representation of density differences in a sample or, in other words, to obtain a 3D reconstruction of a porous object, but also may serve to extract quantitative bulk properties, such as particle size distributions, pore volume, and pore-size distribution. The values extracted from the CT measurements match very well the data measured by conventional methods. However, there are several problems with the extraction of bulk data from CT-data.

(1) Contrast thresholding remains a time-consuming

https://doi.org/10.1557/jmr.2007.0181

processing step, which is also a considerable source of errors.

(2) To keep computer processing time reasonable, the volume of the sample (VOI) that can be processed must be limited.

(3) Cutting effects at the boundaries of the VOIs induce errors in bulk data. The nature and the extent of the errors, however, is predictable. All these drawbacks are, however, made relative by the fact, that CT leaves the samples intact.

ACKNOWLEDGMENTS

The authors would like to thank Dr. Benita Putlitz, Susanne Skora, and Thomas Müller for the assistance and use of the x-ray microtomography equipment at the University of Lausanne.

REFERENCES

1. D.B. Miracle: Metal matrix composites—From science to technological significance. *Comp. Sci. Technol.* **65,** 2526 (2005).
2. M.N. Rittner: *Metal Matrix Composites in the 21st Century: Markets and Opportunities* (GB-108R, BCC, Inc., Brownfield, TX, 2000), p. 184.
3. A. Evans, C. San Marchi, and A. Mortensen: *Metal Matrix Composites in Industry—An Introduction and a Survey* (Kluwer Academic Publishers, Dordrecht, The Netherlands, 2003), p. 423.
4. N. Eustathopoulos and A. Mortensen: Capillary phenomena, interfacial bonding and reactivity, in *Fundamentals of Metal Matrix Composites*, edited by S. Suresh, A. Mortensen, and A. Needleman (Butterworth-Heinemann, Stoneham, UK, 1993), p. 42.
5. M. Rosso: Ceramic and metal matrix composites: Routes and properties. *J. Mater. Proc. Technol.* **175,** 364 (2006).
6. F.L. Matthews and R.D. Rawlings: *Composite Materials: Engineering and Science,* 4th ed. (Woodhead Publishing, Cambridge, UK, 2003), p. 470.
7. K. Lemster, U.E. Klotz, S. Fischer, P. Gasser, and J. Kübler: Titanium as an activator material for producing metal matrix composites (MMC) by melt infiltration (Ti-2003, Proc. Conf. Titan. **10,** Wiley VCH, Hamburg, Germany, 2003), pp. 2515–2522.
8. J. Kübler, K. Lemster, P. Gasser, U.E. Klotz, and T. Graule: MMCs by activated melt infiltration: High-melting alloys and oxide ceramics, presented at the 28th International Cocoa Beach Conference and Exposition on Advanced Ceramics & Composites (Cocoa Beach, FL, 2004; unpublished).
9. K. Lemster, T. Graule, and J. Kübler: Processing and microstructure of metal matrix composites prepared by pressureless Ti-activated infiltration using Fe-base and Ni-base alloys. *Mater. Sci. Eng., A* **393,** 229 (2005).
10. N. Eustathopoulos and B. Drevet: Determination of the nature of metal–oxide interfacial interactions from sessile drop data. *Mater. Sci. Eng., A* **249,** 176 (1998).
11. N. Eustathopoulos, M.G. Nicholas, and B. Drevet: *Wettability at High Temperatures,* Pergamon Material Series, Vol. 3, edited by R.W. Cahn (Pergamon, Oxford, UK, 1999), p. 106.
12. E. Saiz, R.M. Cannon, and A.P. Tomsia: Reactive spreading: Adsorption, ridging and compound formation. *Acta Mater.* **48,** 4449 (2000).
13. C. Wan, P. Kristalis, B. Drevet, and N. Eustathopoulos: Optimization of wettability and adhesion in reactive nickel-based alloys/alumina systems by a thermodynamic approach. *Mater. Sci. Eng., A* **207,** 181 (1996).
14. M.J. Moura, P.J. Ferreira, and M.M. Figueiro: Mercury intrusion porosimetry in pulp and paper technology. *Powder Technol.* **160,** 61 (2005).
15. A. Carlos and Léon y Léon: New perspectives in mercury porosimetry. *Adv. Colloid Interface Sci.* **76–77,** 341 (1998).
16. L. Palacio, P. Pradanos, and J.I. Calvo: Porosity measurements by a gas penetration method and other techniques applied to membrane characterization. *Thin Solid Films* **348,** 22 (1999).
17. V. Karageorgiou and D. Kaplan: Porosity of 3D biomaterial scaffolds and osteogenesis. *Biomaterials* **26,** 5474 (2005).
18. R.A. Cook and K.C. Hover: Mercury porosimetry of hardened cement pastes. *Cem. Concr. Res.* **29,** 933 (1999).
19. G. de With and H.J. Glass: Reliability and reproducibility of mercury intrusion porosimetry. *J. Eur. Ceram. Soc.* **17,** 753 (1997).
20. Y.M. Chiang, D.P. Birnie III, and W.D. Kingery: Principles for ceramic science and engineering, in *Physical Ceramics,* edited by C. Robichaud (John Wiley & Sons, Brisbane, Australia 1997) p. 263.
21. Y. Wu, G.S.P. Castle, and I.I. Inculet: Particle size analysis in the study of induction charging of granular materials. *J. Electrost.* **63,** 189 (2005).
22. O. Gauthier, R. Mueller, D. von Stechow, B. Lamy, P. Weiss, J.M. Bouler, E. Aguado, and G. Daculsi: In vivo bone regeneration with injectable calcium phosphate biomaterial: A three-dimensional micro-computed tomographic, biomechanical and SEM study. *Biomaterials* **26,** 5444 (2005).
23. K. Belaroui, M.N. Pons, and H. Vivier: Morphological characterization of gibbsite and alumina. *Powder Technol.* **127,** 246 (2002).
24. R. Xu and O.A. di Guida: Comparison of sizing small particles using different technologies. *Powder Technol.* **132,** 145 (2003).
25. M.A. Schiavon, E. Radovanovic, and I.V.P. Yoshida: Microstructural characterization of monolithic ceramic-matrix composites from polysiloxane SiC powder. *Powder Technol.* **123,** 232 (2002).
26. Z. Ma, H.G. Merkus, J.G.A.E. de Smet, C. Heffels, and B. Scarlett: New developments in particle characterization by laser diffraction: Size and shape. *Powder Technol.* **111,** 66 (2000).
27. S. Igarashi, A. Watanabe, and M. Kawamura: Evaluation of capillary pore size characteristics in high-strength concrete at early ages. *Cem. Concr. Res.* **35,** 513 (2005).
28. S. Brunauer, Ph. Emmett, and E. Teller: Adsorption of gases in multimolecular layers. *J. Am. Ceram. Soc.* **60,** 309 (1938).
29. I. Langmuir: Vapor pressures, evaporation, condensation and adsorption. *J. Am. Ceram. Soc.* **54,** 2798 (1932).
30. R. Yang and N.R. Buenfeld: Binary segmentation of aggregate in SEM image analysis of concrete. *Cem. Concr. Res.* **31,** 437 (2001).
31. S.T. Ho and W.A. Hutmacher: A comparison of micro CT with other techniques used in the characterization of scaffolds. *Biomaterials* **27,** 1362 (2006).
32. J. Matejicek, B. Kolman, J. Dubsky, K. Neufuss, N. Hopkins, and J. Zwick: Alternative methods for determination of composition and porosity in abradable materials. *Mater. Charact.* **57,** 17 (2006).
33. L. Farber, G. Tardos, and J.N. Michaels: Use of x-ray tomography to study the porosity and morphology of granules. *Powder Technol.* **132,** 57 (2003).
34. S. Blacher, A. Leonard, B. Heinrichs, N. Tcherkassova, F. Ferauche, M. Crine, P. Marchot, E. Loukine, and J.P. Pirard: Image analysis of x-ray microtomograms of Pd–Ag/SiO_2 xerogel catalysts supported on Al_2O_3 foams. *Colloid Surf. A-Physicochem. Eng. Asp.* **241,** 201 (2004).
35. I.G. Watson, M.F. Forster, P.D. Lee, R.J. Dashwood, R.W. Hamilton,

and A. Chrazi: Investigation of the clustering behaviour of titanium diboride particles in aluminium. *Compos. Pt. A-Appl. Sci. Manuf. Investigation* **26,** 1177 (2005).
36. A. Velhinho, P.D. Sequeira, R. Martins, G. Vignoles, F.B. Fernandes, J.D. Botas, and L.A. Rocha: X-ray tomographic imaging of Al/SiC_p functionally graded composites fabricated by centrifugal casting. *Nucl. Instrum. Methods Phys. Res. Sect. B-Beam Interact Mater. Atoms* **200,** 295 (2003).
37. A. Borbély, F.F. Csikor, S. Zabler, P. Cloetens, and H. Biermann: Three-dimensional characterization of the microstructure of a metal-matrix composite by holotomography. *Mater. Sci. Eng., A* **367,** 40 (2006).
38. R.A. Ketcham and W.D. Carlson: Acquisition, optimization and interpretation of x-ray computed tomographic imaginery: Applications to the geosciences. *Comput. Geosci.* **27,** 381 (2001).
39. C.L. Lin and J.D. Miller: Pore structure and network analysis of filter cake. *Powder Technol.* **154,** 61 (2005).
40. E. Masad, S. Saadeh, T. Al-Rousan, T.E. Garboczi, and D. Little: Computations of particle surface characteristics using optical and x-ray CT images. *Comput. Mater. Sci.* **34,** 406 (2005).
41. E. Maire, A. Fazekas, L. Salvo, R. Dendievel, S. Youssef, P. Cloetens, and J.M. Letang: X-ray tomography applied to the characterization of cellular materials: Related finite element modelling problems. *Compos. Sci. Technol.* **63,** 2431 (2003).
42. A.A. Proussevitch and D.L. Saghagian: Recognition and separation of dicrete objects within complex 3D voxelized structures. *Comput. Geosci.* **27,** 441 (2001).
43. M. Coster and J.L. Chermant: Image analysis and mathematical morphology for civil engineering materials. *Cem. Concr. Compos.* **23,** 133 (2001).
44. F. Natterer: Numerical methods in tomography. *Acta Numerica* **8,** 107 (1999).
45. L. Salvo, P. Cloetens, E. Maire, S. Zabler, J.J. Blandin, J.Y. Buffière, W. Ludwig, E. Boller, D. Bellet, and C. Josserond: X-ray micro-tomography an attractive characterization technique in material science. *Nucl. Instrum. Methods Phys. Res. Sect. B–Beam Interact. Mater. Atoms* **200,** 273 (2003).
46. E.E. Underwood: *Quantitative Stereology* (Addison-Wesley, Reading, MA, 1970).
47. A. Saotome, R. Yoshinaka, M. Osada, and H. Sugiyama: Constituent material properties and clast-size distribution of volcanic breccia. *Eng. Geol.* **64,** 1 (2002).
48. L.A. Feldkamp, L.C. Davis, and J.W. Kress: Practical cone-beam algorithm. *J. Opt. Soc. Am. A* **1,** 612 (1984).
49. Y.H. Xu and H.C. Pitot: An improved stereologic method for three-dimensional estimation of particle size distribution from observations in two dimensions and its application. *Comp. Meth.* **72,** 1 (2003).

https://doi.org/10.1557/jmr.2007.0181